Regional-scale bridge condition monitoring using InSAR displacements and environmental data

Regional-scale bridge condition monitoring using InSAR displacements and environmental data

Said Quqa[1]*, Antonio Palermo[1], Francesco Ubertini[1], and Alessandro Marzani[1]

Abstract

This paper introduces a novel methodology for detecting and classifying anomalies in multiple bridges within a geographical region using satellite-based interferometric synthetic aperture radar (InSAR) displacements and environmental measures. The approach uses subspace alignment to harmonize bridge features, enabling the detection of anomalies based on deviations in one bridge compared to the rest of the population. Simulated and real case studies involving steel railway bridges spanning the Po River in Italy demonstrate the effectiveness of the proposed approach, showcasing its potential for large-scale applications. Moreover, the study explores the transferability of knowledge from simulated data to real-world monitoring scenarios, yielding promising results in classifying real instances using synthetic labels. The proposed approach presents practical benefits for bridge monitoring agencies by providing a cost-effective method for enhancing the resilience and safety of transportation infrastructure.

Keywords

population-based structural health monitoring, transfer learning, remote sensing, damage identification, climate change, scour

Introduction

Recent progress in managing transportation infrastructure increasingly relies on data-driven approaches, using sophisticated integration techniques that lean towards the emerging concept of "digital twin" (1). Initially proposed for individual structures, digital twins have recently expanded to encompass entire regions (2). They aim to model the complex relationships between multiple structures and infrastructures, their inputs, and the consequences of failure and performance reductions of critical elements. This modeling proves invaluable for assessing the resilience of transportation networks, a topic gaining significant traction due to well-documented recent climate-related emergencies (3).

Among the crucial components of transportation networks, bridges hold paramount importance. Monitoring bridge conditions typically requires extensive sensing (4). However, the abundance of sensors entails considerable deployment, maintenance, and management costs. To tackle these challenges, ongoing research in bridge structural health monitoring (SHM) is shifting towards cost-effective data acquisition technologies. These include remote satellite-based sensing, which eliminates the need for installing on-site sensors.

Notably, synthetic aperture radar interferometry (InSAR), initially employed for monitoring land movements, has recently achieved remarkable sensitivity owing to evolving technologies (5). This approach leverages synthetic aperture radar (SAR) devices aboard orbiting satellites to deliver high-resolution, weather-independent imagery of the Earth's surface. Various natural and man-made structures, such as rocks, building roofs, and road surfaces, strongly reflect the electromagnetic signals emitted by radars, which capture the back-scattered signals, thus generating SAR images. Displacement time series for specific reflective elements, known as persistent scatterers (PSs), can then be obtained by applying specific algorithms on multiple images, achieving millimetric precision along the line of sight (LOS) connecting the SAR sensor to these points (6).

Due to its high sensitivity, this strategy has recently been exploited for static monitoring of several civil structures, such as bridges. Significant advantages include the widespread availability of data – virtually, from the entire globe – and access to historical records – now spanning over a decade. Consequently, it enables investigations into the causes behind structural issues in bridges that were never equipped with dedicated sensing systems (7; 8; 9; 10; 11; 12; 13). Since the displacement measurements obtained via InSAR are static, the types of damage that can be identified remotely include scouring/erosion effects (10; 11; 14), differential displacements due to local settlements (12; 13; 15), land subsidence/uplift (7; 16), and deck deformation (8; 9). Literature contributions in this field also analyze bridge deformation induced by seasonal thermal effects, which exhibit a characteristic fluctuating pattern with a yearly cycle (17; 18; 19; 20; 21; 22; 23; 24), and the correlation between displacements and water levels (25; 26; 27; 28). In addition, InSAR-based monitoring has become particularly appealing for monitoring infrastructure networks in wide geographical regions (29).

[1]University of Bologna, Viale del Risorgimento 2, Bologna, 40136, Italy

Corresponding author:

*Said Quqa, University of Bologna, Viale del Risorgimento 2, Bologna, 40136, Italy

Email: said.quqa2@unibo.it

In the current literature, scholars have demonstrated how InSAR data can complement or precede SHM strategies based on on-site systems, noting that both methods generally align in measuring displacement trends, though satellite measurements may sometimes be unavailable for specific structures or less accurate than field measurements (30; 31). Additionally, methods traditionally used for on-site monitoring have been applied to InSAR data to detect anomalous behavior of different types of structures. For instance, Bonaldo et al. (32) analyzed the residuals of autoregressive models trained on 3 years of multi-temporal (MT)-InSAR displacement data obtained from COSMO-SkyMed images to detect anomalies for Palazzo Primoli in Rome (Italy). Selvakumaran et al. (10) processed several TerraSAR-X images over the Tadcaster Bridge (England), highlighting the reliability of MT-InSAR methods to identify anomalous displacements in a region of the bridge where partial collapse occurred due to scour. Similarly, Sousa and Bastos (11) used MT-InSAR data to study the displacement time history that preceded the collapse of the Hintze Ribeiro bridge across the Douro River. The authors confirmed the possibility of implementing an early warning system based on the definition of displacement alarm thresholds based on static remote measurements. Also, Cusson et al. (33) employed satellite monitoring as an early warning mechanism for unexpected displacements. De DePrekel et al. (34) investigated the gradual displacement of some bridges in California, attributing the movements to subsidence phenomena resulting from continuous water extraction from nearby aquifers. Milillo et al. (8) discussed relative deformations of the Morandi Bridge (Italy) recorded before its collapse in 2018.

An effort to reconstruct the two-dimensional displacement field was undertaken by Farneti et al. (12), gathering displacement data from both ascending and descending geometries for the Albiano-Magra viaduct, which collapsed in 2020. The authors also analyzed the displacements of surrounding areas, which provided key information for determining the possible causes of the collapse. In a following study, Farneti et al. (13) combined the information obtained through InSAR measurements with numerical modeling to predict the service life of the Albiano-Magra viaduct. Lately, several scholars have employed numerical models to help interpret or predict displacement trends of monitored structures and to calibrate structural properties. Vázquez-Ontiveros et al. (35) assessed the risk of dam failure by monitoring radial displacements at various reservoir levels, using refined finite element (FE) models for interpretation. Similarly, Guzman-Acevedo et al. (36) proposed a risk assessment methodology to estimate a safety index of bridges using InSAR data and a calibrated FE model based on stress limits provided by the American Association of State Highway and Transportation Officials (AASHTO). Zhou et al. (37) obtained an advanced temperature field model within the elements of a steel arch bridge using meteorological data available online, including temperature, wind speed, and precipitation. The authors used both environmental and InSAR data to refine the thermal dilation phase in their bridge model.

Typically, prior knowledge of structures is required to develop the models used in these studies for reliably interpreting InSAR measurement results (30). Additionally, most of the referenced papers focus on individual bridges, comparing their current state with their past behavior to identify any variations potentially linked to damage. This approach is commonly employed in civil SHM. The inherent dissimilarities among different bridges prevent the direct comparison between their behaviors to detect anomalies. Conversely, direct comparison is frequently used in fault detection within other domains, such as mechanical engineering, for identical machinery components.

Recently, population-based SHM (PBSHM) has emerged as a strategy to transfer knowledge across various bridges deemed sufficiently ”similar” (38). This approach aims to infer damage classification information by leveraging data from bridges with documented similar behaviors (39). In civil engineering, this is mainly achieved through domain adaptation (DA) algorithms. DA, a specific type of transfer learning method, addresses discrepancies between ”source” and ”target” features (i.e., parameters that describe the structural behavior) with distinct marginal and class-conditional distributions, aiming to minimize their disparity (40). Consequently, aligned features can train damage classifiers applicable to both the source and target structures.

To date, PBSHM has predominantly focused on dynamic features. Gardner et al. (41) explored DA concepts for vibration-based SHM in multi-story buildings. In the realm of bridge SHM, Poole et al. (42) used statistic alignment, one of the simplest DA techniques, to align natural frequencies from different bridges, namely, the Z24 and KW51 bridges, showcasing its efficacy in recognizing environmental variations. Similarly, Giglioni et al. (39) demonstrated improved damage detection by applying different DA methods between the Z24 and S101 bridges. Omori Yano et al. (43) employed various transfer learning strategies across bridges, including transfer component analysis (TCA), joint domain adaptation, and maximum independence domain adaptation. Additionally, Figueiredo et al. (44) proposed employing TCA to harmonize classifiers between real bridge data and simplified numerical models.

The widespread availability of satellite data facilitates the acquisition of datasets encompassing a vast array of similar bridges in large regions. Additionally, access to historical data renders alignment strategies and DA approaches accessible. Nevertheless, static measures have never been explored for damage-related knowledge transfer. Therefore, novel features must be devised to be damage-sensitive (considering the types of damage observable through InSAR data) and maintain consistency across bridges (irrespective of the number of PSs identified by the InSAR methods) when transfer learning algorithms are applied.

This study introduces an innovative approach to anomaly detection and characterization that reduces reliance on past experiences of monitored structures. This aspect is critical in light of climate change and the rising frequency of severe weather events, aiming to mitigate the risk of false alarms stemming from environmental factors previously unencountered by the monitored bridges (45).

Specifically, the study proposes a methodology for ”regional-scale” SHM, which addresses a typical challenge faced by management administrations that cannot afford to instrument all bridges in their area of interest but require data

for territorial analyses, such as evaluation of the resilience of the transportation network. The proposed methodology considers a population of similar bridges within a confined geographical area. The underlying assumption is that these bridges share similar structural properties (i.e., geometry and boundary conditions) and environmental factors influencing their static response, such as temperature variations and the fact that they traverse the same river.

The proposed strategy is finalized to detect anomalous bridge displacements, which may potentially lead to failure mechanisms. It operates on the premise that bridges with similar designs and environmental drivers should exhibit comparable structural responses over time. However, direct comparisons in physical space are hindered by the unique characteristics of each bridge. To address this challenge, this study proposes using SA to render bridge static features comparable within a latent domain shared by all bridges. An anomaly index is then defined in this domain based on instantaneous differences between bridge behaviors. Next, a methodology for inferring information about the type of anomaly is introduced, using synthetic bridge models for simulation-to-real knowledge transfer. The feasibility of a meaningful knowledge transfer relies on the similarity between the developed models and real bridges, which share common features, including structural schemes and dimensions, riverbed topography, and environmental conditions.

This approach introduces the following key innovations: (1) it applies PBSHM to InSAR data for the first time, defining a tailored set of static damage-sensitive features; (2) it shifts monitoring from individual time-based comparisons to relative instantaneous comparisons, reducing the dependence on historical data; and (3) it relies solely on publicly available data (InSAR and environmental measures) accessible online, potentially applicable to bridges worldwide.

The next section outlines the proposed methodology for regional-scale bridge monitoring and introduces the selected case study and the data employed in this research. The approach is then demonstrated using simplified bridge models to simulate various types of anomalies, both physical and computational. Finally, the proposed method is applied to a real case study involving a population of seven steel railway bridges spanning the Po River in Italy. Final remarks are drawn in the Conclusions.

Regional-scale bridge monitoring

In traditional SHM procedures, when real-world environmental conditions differ from those used to train anomaly detection models, false positives can occur due to unexpected data trends (46; 47). This study introduces a method that compares the responses of similar bridges to shared environmental inputs. Given the low likelihood of all bridges experiencing structural anomalies simultaneously, if multiple bridges exhibit behavior that deviates from their historical patterns, it is more probable that the anomaly is due to an unusual environmental driver. Conversely, actual anomalies are identified if only a small subset of bridges reacts differently from the rest under the same environmental inputs. This approach helps minimize false alarms. Since environmental inputs are not identical for all monitored structures, and their responses may vary depending on the individual bridge characteristics, a DA process is applied to pre-process the bridge features.

The proposed methodology consists of the following steps:

1. Similarity assessment: A population of bridges is formed according to similarity criteria regarding their structural behavior.
2. Initialization and feature extraction: All available datasets (in this study, displacement and environmental data) are encoded into standardized structural features and projected onto a common latent domain using DA.
3. Anomaly detection: Abnormal behaviors within one or more bridges are identified using a damage indicator that considers the disparities between the behavior of bridge features in the latent domain.
4. Anomaly characterization: The features of anomalous bridges are classified using a machine learning-based model trained on ”source” bridge(s) with available anomaly labels.

This method assumes that a set of anomalous behaviors has already been recognized and labeled for the source bridges. This recognition may involve interpreting data from additional sensors (such as dynamic sensing systems, strain gauges, or riverbed level sensors) or conducting visual inspections to validate anomalous conditions that may have occurred in the past. The gathered information is then transferred from the source domain to the target domain, which includes bridges with limited knowledge regarding their condition. Noteworthy, if labels are not initially available for any bridges in the population, they can be assigned during the monitoring process as soon as a new anomaly is detected and validated through visual inspections or professional interpretations involving a human-in-the-loop process (48). This allows for the continual enrichment of the label database throughout the monitoring lifespan, gathering labels for various phenomena that may impact any bridge within the population.

Similarity assessment

Recent research has delved into the prerequisites necessary for structures within a population to achieve ”positive transfer”, whereby knowledge transfer effectively enhances anomaly classification outcomes. In this regard, scholars have proposed a method of conceptualizing structures using irreducible element (IE) models, which are simplified representations of structural components, and encoding them into attributed graphs (AGs) (38). AGs consist of compact representations of the connections between elements alongside their pertinent information, such as material, size, and shape. This process becomes crucial when the features used in anomaly identification are closely linked to these characteristics and are sensitive to their variations. For instance, in studies that use natural frequencies for vibration-based PBSHM, it is fundamental to ensure similarity in connections, material properties, and geometric characteristics, all of which influence the mass and stiffness of the systems.

This study uses structural features derived from static displacement measures to identify structural anomalies (i.e., excessive displacements) potentially related to incipient failure mechanisms in statically determinate structures. As a result, material properties and cross-section geometry become less significant. Conversely, ensuring consistency in the structural configuration (i.e., the connections between decks and piers) in all bridges within the population is essential.

Thus, the similarity assessment needed by the proposed approach is less stringent than the one commonly employed for vibration-based problems, prompting avenues for further exploration. Future studies will pursue specific investigations in this direction.

The case study investigated in this paper comprises seven railway steel bridges (B1-B7) spanning the Po River in Italy, depicted in Fig. 1. All these bridges consist of simply supported truss elements supported by piles, some of which are located within the river. Additionally, the bridge spans are of similar lengths, ranging approximately between 65m and 85m. Consequently, the bridges in this case study have comparable structural configurations and face similar environmental conditions, as detailed in the following sections.

Initialization and feature extraction

The displacement data used in this study consists of InSAR Sentinel-1 data, post-processed to derive purely vertical displacement components at a regular grid of control points. This data was acquired by fusing PSs identified from ascending and descending orbit satellites and interpolating measurements to a 100m grid. This study did not involve the extraction of displacement time histories from SAR images. Instead, the displacement data were sourced from the European Ground Motion Service (EGMS) as part of the Copernicus project (49). Comprehensive details regarding the algorithms and parameters used to generate this data are available in the EGMS technical documentation (50). The employed data spans two time intervals: (I1) January 5, 2016, to December 22, 2021, and (I2) January 6, 2018, to December 17, 2022. Displacement time histories for these intervals were obtained individually from different InSAR image sets, causing non-coincidence in the data during the overlapping period. The original sampling period of both displacement datasets is every 6 days. The displacement data refers to the control points depicted in Fig. 2. Specifically, the number of control points extracted for bridges B1-B7 are 7, 11, 4, 9, 14, 12, and 11, respectively. Bridge areas that delimit the employed control points were defined manually.

The displacements at control points represent an average quantity estimated within the respective grid element with millimeter-level accuracy (50). However, it is crucial to note that vegetation and water do not generate PSs. Consequently, the control points available are likely only representative of the bridge movements.

Environmental data analyzed in this paper encompass air temperature, water level, and water discharge measured close to the selected bridges. Specifically, air temperature 2m above the land surface was sourced from ERA5-Land Copernicus datasets (51). These datasets are available at a 10 km grid and hourly time discretization. Water level information was obtained from hydrographic monitoring stations managed by the Interregional Agency for the Po River (AIPo), accessible online via the agency website (52). Sampling periods for water level vary between 5 and 10 minutes depending on the specific monitoring station. Water discharge data near selected bridges was obtained from the Dext3r service, a web system provided by the Regional Agency for Prevention, Environment, and Energy of Emilia-Romagna (ARPAE) (53). Environmental data was acquired for the entire time interval enclosing I1 and I2, as depicted in Fig. 3. Noteworthy, air temperatures and the water discharge observed for all the considered bridges exhibit remarkable similarities.

The first step of data initialization involves resampling the displacement and environmental data onto a fixed temporal grid. This is achieved by applying linear interpolation to displacement data to obtain a daily sampling period. On the other hand, environmental data was first processed through a moving average process with a 1-day window and then subsampled to have the same sampling period as displacement data.

In this process, two distinct datasets were created: the first spans from January 5, 2016, to November 13, 2019 (using InSAR data from I1), and the second spans from November 14, 2019, to December 17, 2022 (using InSAR data from I2). In the following, these datasets are termed the ”reference” and ”monitoring” time intervals, respectively.

Upon resampling, a set of features is extracted from the data. Due to limitations inherent to InSAR technology and displacement extraction algorithms, the displacement time histories are not tied to specific locations on the selected bridges but should be understood as average displacements (with associated uncertainties) within each square area of the 100m grid. This introduces two main challenges for feature extraction: (1) different bridges typically have varying numbers of control points, and (2) it is impossible, with the data type used in this study, to reference displacements to a specific part of the structure. Nonetheless, these displacements can effectively capture the overall behavior of the structure on a scale roughly equivalent to its span size. These constraints led to defining features that condense the information into global indicators, such as average displacements and the distribution of displacements at control points relative to the average (i.e., statistical moments). Specifically, this study proposes the features listed in Tab. 1. In defining them, four possible anomalies were considered: scouring (Sc) processes, which typically result in global stiffness reductions in pier foundations due to vortexes that lower the riverbed depending on water speed and bridge geometry (54; 55); differential settlements (Se), involving anelastic displacement of selected piers downwards; uplifts (Up), similar to settlements but involving upward displacements; and outliers (Ou), a typical anomaly associated with InSAR data, for instance, due to changes of a PS from one physical element to another within the spatial grid.

The features outlined in Tab. 1 pose challenges for direct comparison across different bridges due to inherent differences between the individuals of the population, i.e., the features (f_k) of different datasets have different marginal distributions. Hence, subspace alignment (SA) (56), a DA

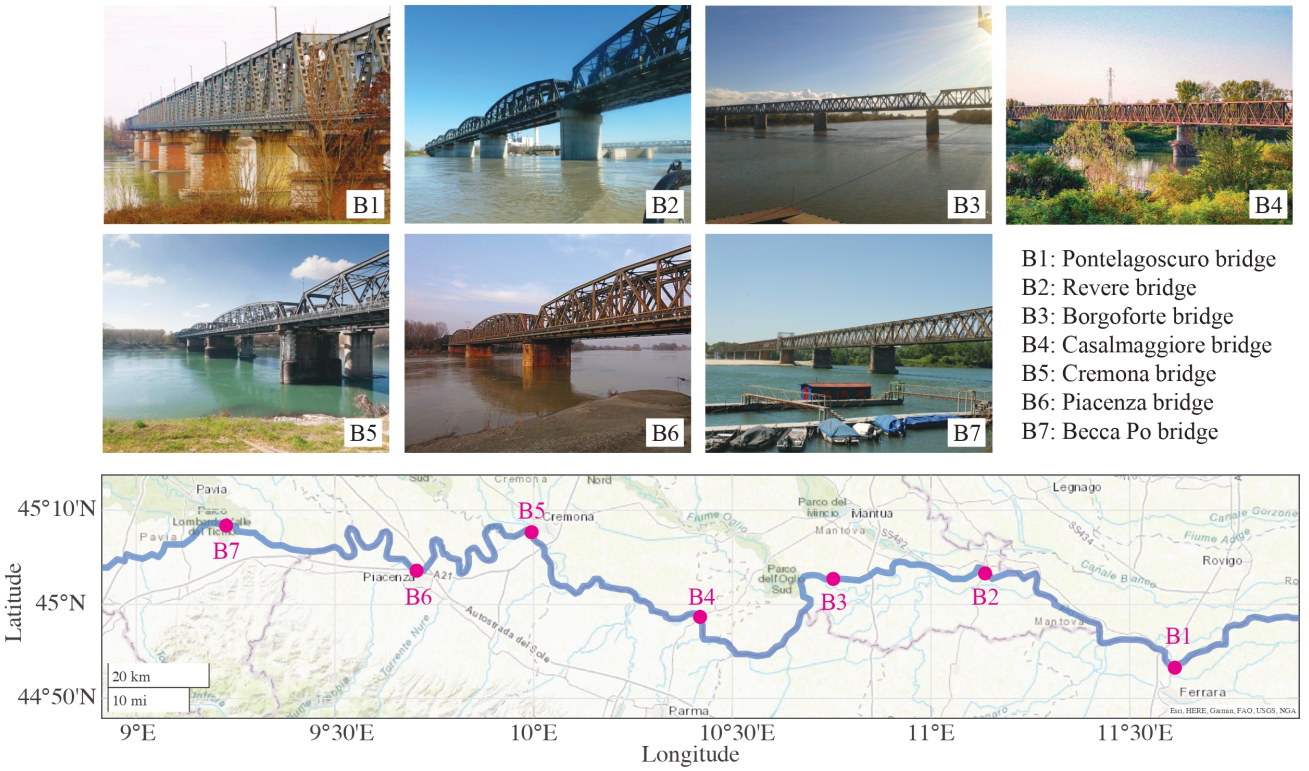

Figure 1. Selected case study on the Po River, Italy.

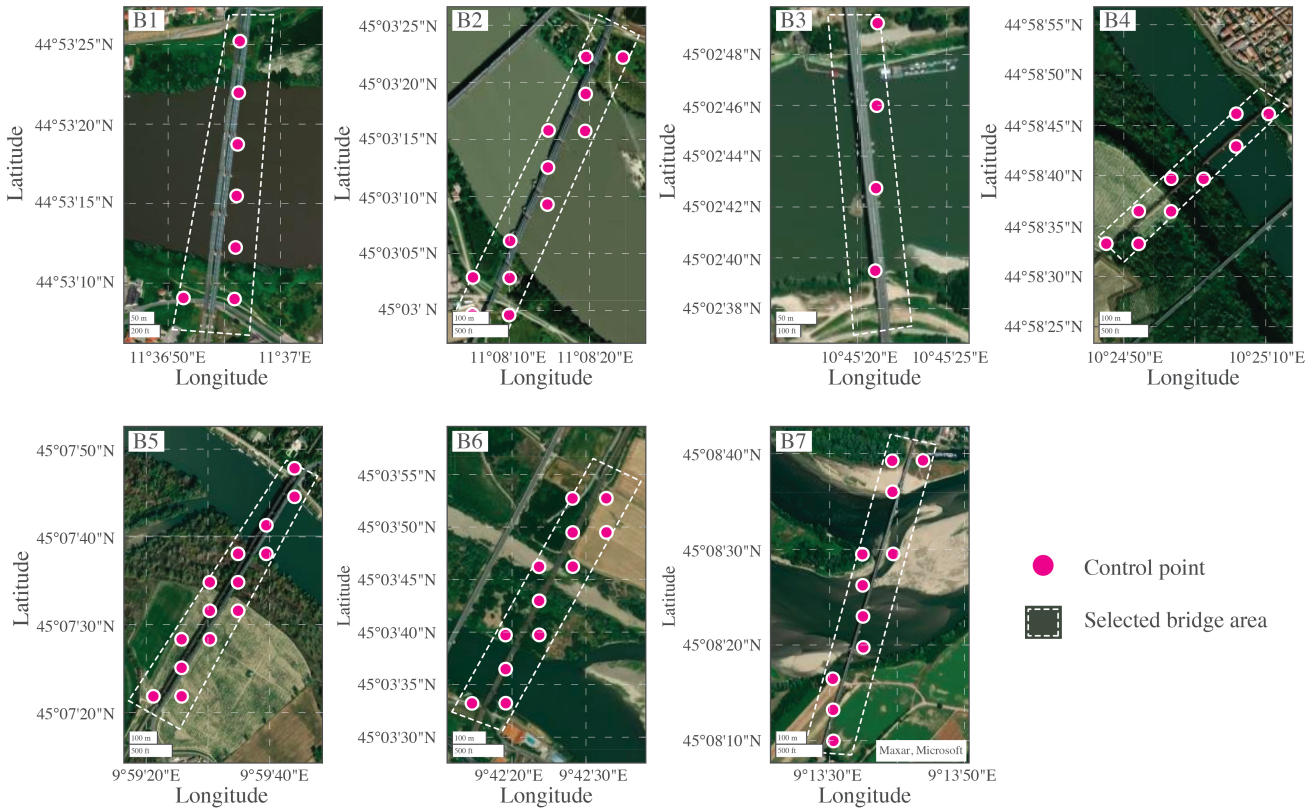

Figure 2. Satellite views of the selected bridges and control points for vertical displacements.

algorithm, is employed to project all features from the source and the target bridges onto a latent domain defined by the principal components of the data of the source bridge(s). Due to this projection, the features of all bridges will overlap in the latent domain. Potentially, these overlaps can also be employed to characterize the identified anomalies, exploiting damage information possibly known from the source domain (e.g., if there is documentation on the source bridges experiencing scour in the past). The general SA process is schematized in Fig 4.

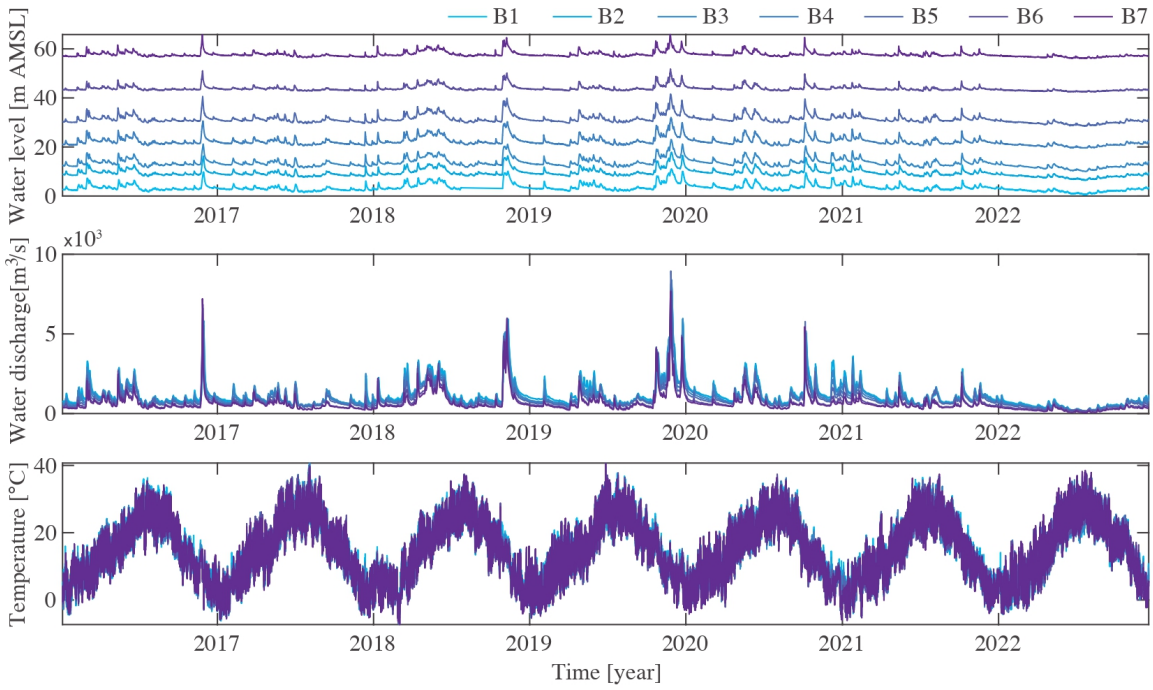

Figure 3. Environmental measurements taken for the selected bridges in the analyzed time interval.

Table 1. Set of proposed physical features.

Feature	Description
f_1	Mean value of the instantaneous vertical displacements
f_2	Standard deviation of the instantaneous vertical displacements
f_3	Distribution skewness of the instantaneous vertical displacements
f_4	Distribution kurtosis of the instantaneous vertical displacements
f_5	Median of the instantaneous vertical displacements
f_6	Minimum value of the instantaneous vertical displacements
f_7	Maximum value of the instantaneous vertical displacements
f_8	Vertical displacement component with maximum variance over the analyzed interval
f_9	Air temperature of the bridge area estimated 2m above the land surface
f_{10}	Water level measured with respect to the sensor location

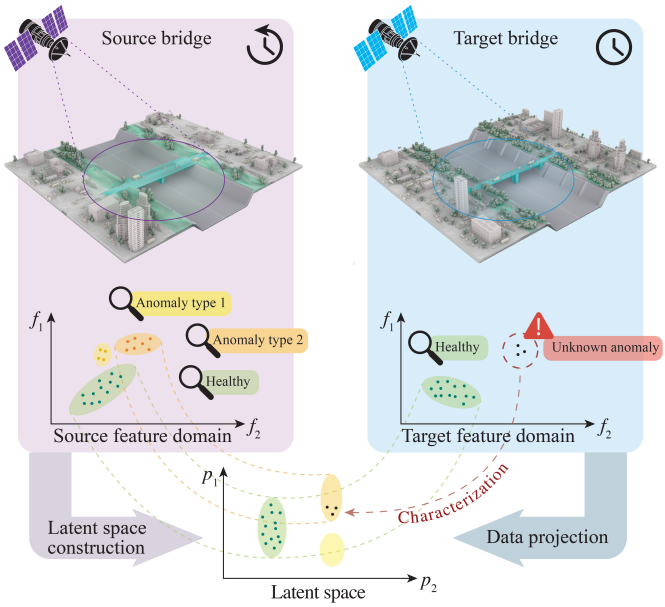

Figure 4. Scheme of the data projection process and anomaly characterization using subspace alignment.

An example of feature distributions before (f_k) and after projection (p_k) is shown in Fig. 5. This figure illustrates the data in the reference interval from three simulated bridges described in the section Simulated benchmark. Specifically, the plots in the gray region show 2D visualizations of the features defined in Tab. 1, while the plots in the red region show 2D visualizations of the projected features p_k.

While extensive details on SA implementation can be found in relevant literature (56), a brief theoretical background is reported herein, together with a scheme that represents its application in the context of this study (see Fig. 6). Let $\mathbf{F}_n \in \mathbb{R}^{D\times K}$ be the physical matrix of features for bridge n, with D denoting the number of instances (i.e., the time extension of the dataset) and K is the number of features (in this case, 10). Here, bridge #1 is considered the source bridge without loss of generality.

First, a mean centering process was applied to every column of $\mathbf{F}_n$. Then, $r \leq K$ principal vectors are extracted from each domain using PCA, corresponding to the r largest principal values. The vectors $\mathbf{V}_n \in \mathbb{R}^{K\times r}$ can thus be seen as a base for each domain. Specifically, $\mathbf{V}_1 \in \mathbb{R}^{K\times r}$ represents a base for the source subspace, while $\mathbf{V}_n \in \mathbb{R}^{K\times r}$ are the bases of the target subspaces (with $n \neq 1$).

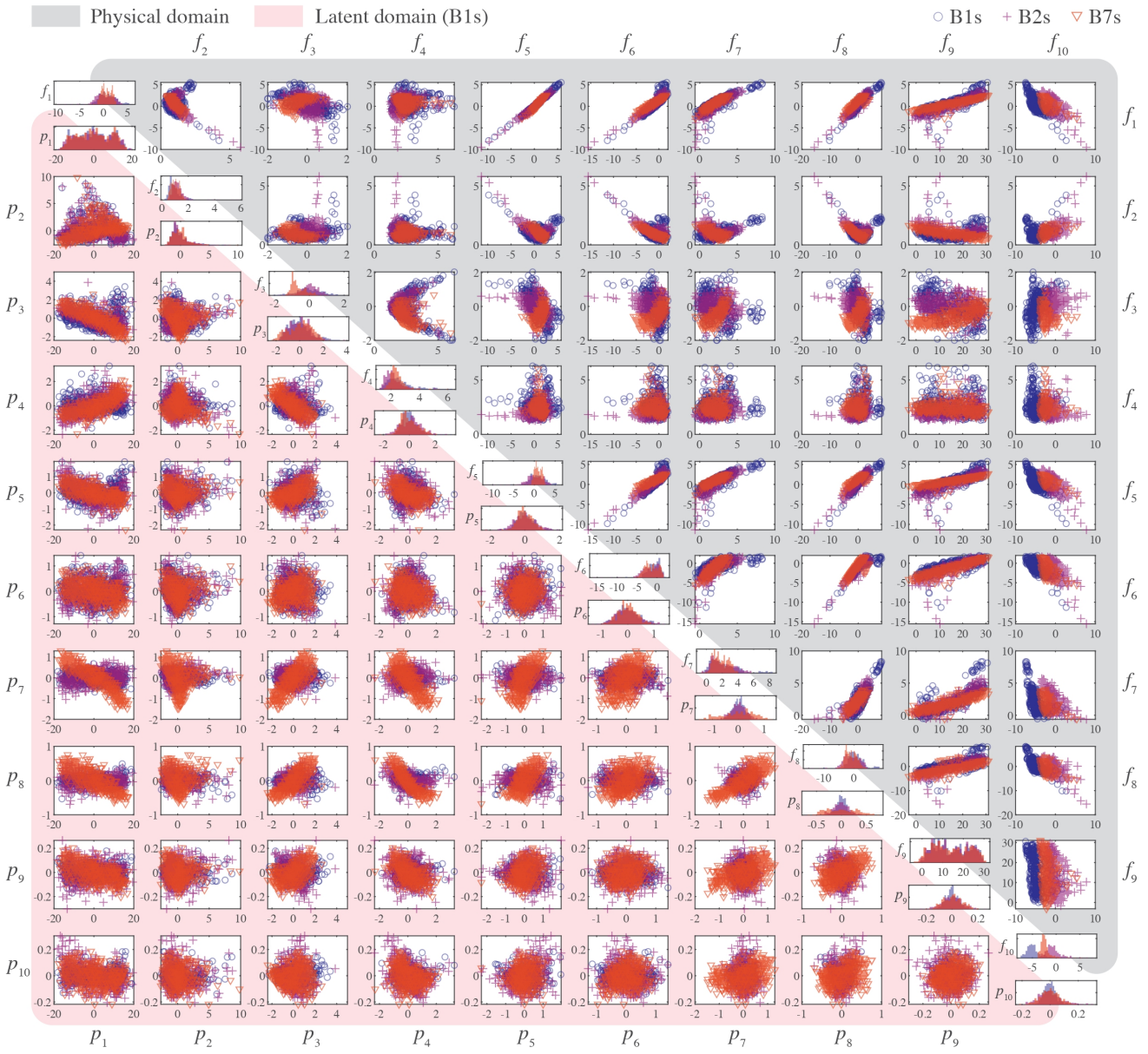

Figure 5. 2D visualizations of the synthetic features of three bridges, namely B1s, B2s, and B7s, before (gray region) and after (red region) projection onto the latent domain (with source B1s) using subspace alignment. The plots on the diagonal represent the probability density distributions of the features.

The target data can thus be projected onto a source-aligned coordinate system according to the projection matrix (56):

$$\mathbf{W}_n = \mathbf{V}_n \mathbf{V}_n^\top \mathbf{V}_1 \tag{1}$$

This matrix transforms the target subspace coordinates into the source subspace coordinates by aligning the target basis vectors with the source ones. Therefore, the source and target data projected onto the source subspace (i.e., the latent space) can be obtained as, respectively:

$$\mathbf{P}_1 = \mathbf{F}_1 \mathbf{V}_1 \tag{2a}$$

$$\mathbf{P}_n = \mathbf{F}_n \mathbf{W}_n \tag{2b}$$

In this study, $r = K$ (i.e., $r = 10$) since dimensionality reduction is not a goal of the proposed method. Due to the similarity in bridge schemes and environmental input, the principal components derived for each bridge should be consistent across the population, as well as the transformation matrices.

The main computational complexity of SA lies in calculating the projection matrices of feature time histories through PCA. This operation has a complexity of $O(KD^2)$ for each bridge, which is relatively limited as the sampling frequency is low for static monitoring applications. Moreover, all computational steps can be easily parallelized across different bridges, making the method easily scalable across wide populations of structures.

It is worth noting that if the projection process is executed during the same reference time interval for all bridges, assumed unaffected by anomalies, the same projection matrices can be used for subsequent monitoring intervals. Furthermore, due to the similarities in environmental drivers, projected features of different bridges should move together in the latent space over time.

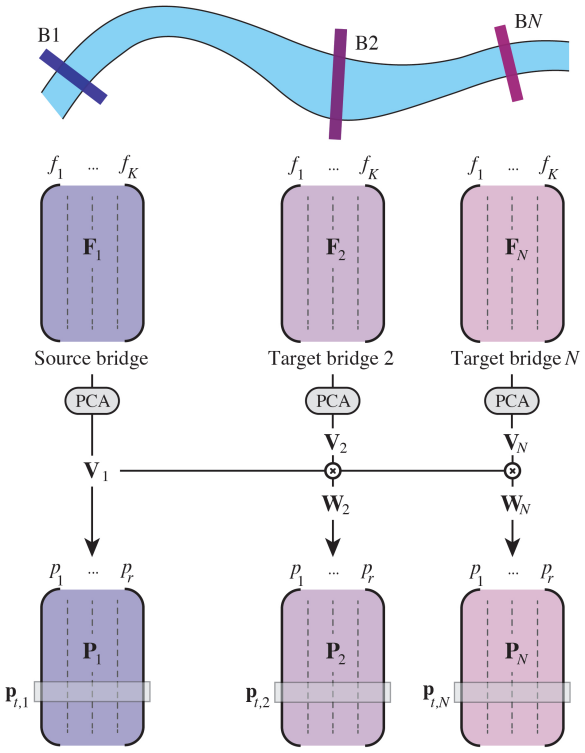

Figure 6. Scheme of the data harmonization process based on subspace alignment.

Anomaly detection

Under regular conditions, the responses of bridges should exhibit similar trajectories within the source subdomain. However, if anomalies occur, denoting changes in the relationship between bridge features, the data from affected bridges would diverge from the average trajectory. This divergence occurs because the original projection matrix cannot accurately represent the new relationship between features. Moreover, if two or more bridges experience the same anomaly, their features should converge to the same region within the source subdomain. Fig. 7 schematizes the proposed anomaly identification process, and in particular, Fig. 7(a) illustrates this situation in a 2D representation of the latent space.

Following this rationale, for each bridge, an anomaly index is defined at time t as the Euclidean distance between a feature point $\mathbf{p}_{t,n}$ and the instantaneous centroid of all instantaneous bridge features $\mathbf{c}_t$ (see Fig. 7(b)):

$$d_{t,n} = ||\hat{\mathbf{p}}_{t,n}|| = ||\mathbf{p}_{t,n} - \mathbf{c}_t|| \tag{3}$$

with $\hat{\mathbf{p}}_{t,n}$ representing the recentered dataset.

Various methods exist for calculating the centroid. In this step, special attention must be given to eliminating anomalous data points, which could affect the detection results. One approach could entail training an autoregressive model with exogenous input to estimate the centroid position at time point t using past instances of displacement-based features and the concurrent influence of exogenous variables (in this case, environmental measures) (57). Alternatively, the implementation of a Kalman filter could be considered, allowing for asynchronous input features without the need for resampling (58). In this study, a straightforward approach is employed to determine the centroid, involving the calculation of the average of all feature points at time point t, with the exclusion of one potential anomalous bridge:

$$\mathbf{c}_t = \frac{1}{N-1} \sum_{n=1}^{N-1} \mathbf{p}_{t,n} \tag{4}$$

where n ranges over all bridges except for the one with the largest Euclidean distance from $\mathbf{c}_t$. Although concurrent anomalies may influence the robustness of this estimate, this method is used in this initial study to showcase the fundamental concept without delving into complex procedures. Forthcoming research will explore more sophisticated methods for centroid calculation.

A threshold for anomaly detection can then be established either by leveraging historical data or employing outlier detection methods based on the instantaneous distribution of distances from the centroid. In the former approach, conventional methods can be used to determine an acceptable probability of false alarms (or errors in damage detection) using data from a reference period. Specific techniques, such as the receiver operating characteristic curve, can aid in determining optimal thresholds (59). Alternatively, reliance on historical data can be entirely eliminated from the methodology in the latter approach. However, a larger population might be required to establish a statistically significant threshold. This study adopts the former approach, acknowledging that dependence on historical data can be removed by increasing the number of bridges within the considered population.

Anomaly characterization

The recentered datasets (denoted as $\hat{\mathbf{P}}_n$ for simplicity), along with available information on the anomalies, can be used to train a classification model capable of labeling newly detected anomalies. Given the unpredictable nature of anomalies, where the number of expected labels cannot be determined in advance, it is crucial that the model can both assign known labels and isolate unknown anomalies from regular data.

This study proposes training a self-organizing map (SOM) (60) with the available data. SOMs are unsupervised learning models commonly used for data visualization, capable of generating low-dimensional representations of high-dimensional data distributions. By creating a SOM with the available dataset, a low-dimensional map with a selected number of nodes and links is formed, where nodes represent centroids of clusters identified in the data. After conducting the unsupervised training process, labeled data can be fed to the SOM to assign relevant labels to the cluster(s) they belong to (see Fig. 7(c)).

Subsequently, unlabeled anomalies can be processed through the SOM. If they are assigned to a cluster with an available label, this label can be used to infer the type of anomaly. On the other hand, if anomalous data are assigned to unlabeled clusters, new labels can be assigned afterward through a human-in-the-loop process involving visual inspections to ascertain the causes behind anomalies on affected bridges.

In contrast to simpler clustering algorithms like k-means, SOMs preserve the topological structure of data, giving

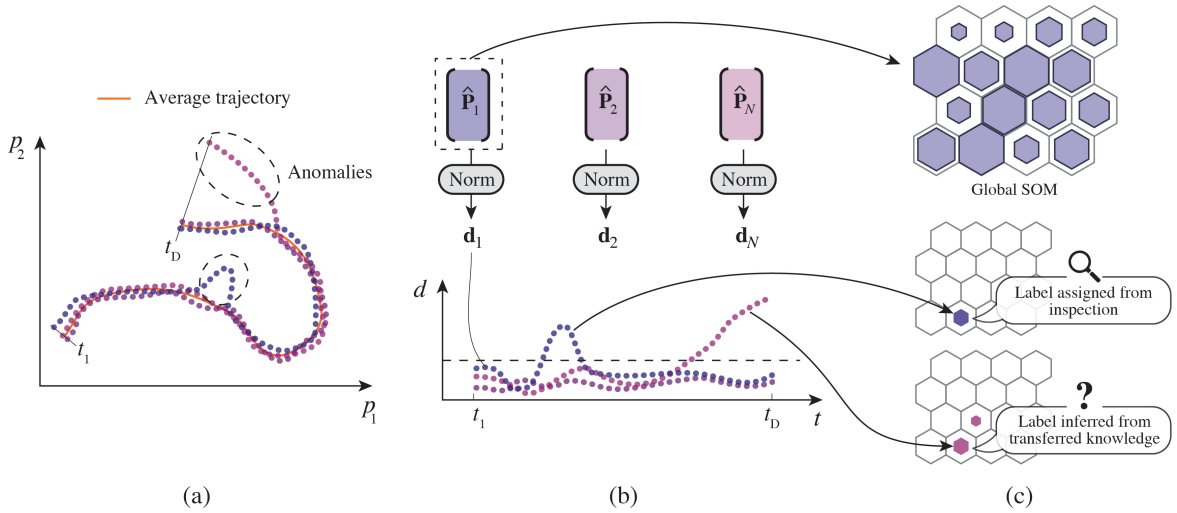

Figure 7. Proposed monitoring workflow: (a) Calculation of the average trajectory; (b) Anomaly detection using the relative distance metric; (c) Anomaly classification using knowledge transfer.

physical meaning to close clusters exhibiting similar features (61). Once trained, the SOM can be deployed for future classification, focusing solely on newly identified anomalies.

Simulated benchmark

An initial demonstration is conducted using numerical models of the bridge population to assess the procedure using known anomalies. Specifically, seven bridges were modeled in 2D, considering the plane orthogonal to the water flow. Here, simulated bridges are labeled as "B#s," while real bridges are denoted as "B#." Despite their simplicity, the models are designed to effectively capture the primary factors influencing the measured structural output, that is, static displacements. The geometric parameters in the developed models closely resemble real-world conditions, while the employed environmental drivers consist of the real measurements described in the section Data description.

Model description

The geometries of the bridges were generated based on topographic measurements of the river sections obtained from the AIPo website (62). While the number and positions of the piles do not precisely replicate the real configurations, they were adjusted to have spans of approximately 72 m, resembling real-world scenarios (63). A schematic representation of the modeled bridges is provided in Fig. 8.

To simulate realistic datasets, actual environmental drivers (i.e., temperature and water level) recorded at the bridge sites were employed. Displacements were derived assuming simply supported and rigid bridge spans, which respond to pier deformations influenced by temperature variations and water level (25; 26). These two environmental drivers were selected based on the high correlation observed with bridge displacements. Specifically, the Pearson correlation coefficient calculated in the reference interval between the average displacement of B1 and the air temperature at that location is 0.701, while it is -0.822 for the average displacement and water level. The model was developed to generate synthetic displacements with similar correlation levels to environmental measures.

A scheme of the model is illustrated in Fig. 9. Piers were modeled as infinitely stiff elements that deform axially in response to temperature changes. The deformation of the point atop the pier was modeled according to the following equation:

$$\delta_T = \alpha_T h \Delta T \tag{5}$$

where h is the height of the considered pier, ΔT is the uniform thermal variation, and α_T is the coefficient of thermal expansion of the pier material. Additionally, the piers are supported by springs representing an equivalent vertical stiffness of the riverbed (k), accounting for complex phenomena that may induce ground deformation, such as seepage through soil layers with different permeability (25). Consequently, the base of the pier experiences vertical translation in response to fluctuating water levels at the pier location (here assumed to have a linear relation with the hydrostatic pressure):

$$\delta_W = -\frac{h_W \gamma_W}{k} \tag{6}$$

in which γ_W is the specific weight of water, while h_W is the water height. Although simplistic, this modeling led to a correlation factor between water level and average vertical displacement similar to the one observed from real data.

The two contributions described above were then combined to provide the total displacement observable on top of the pier due to temperature and water level drivers:

$$\delta = \delta_T + \delta_W \tag{7}$$

The displacements obtained from InSAR data pertain to specific points on the bridge, which may either be PSs or control points that aggregate information from multiple PSs (i.e., the case considered in this study). Consequently, the final displacements of the control points (CP) used in the following analyses were derived as the linear combination of displacements from two consecutive piers (i.e., i and $i+1$):

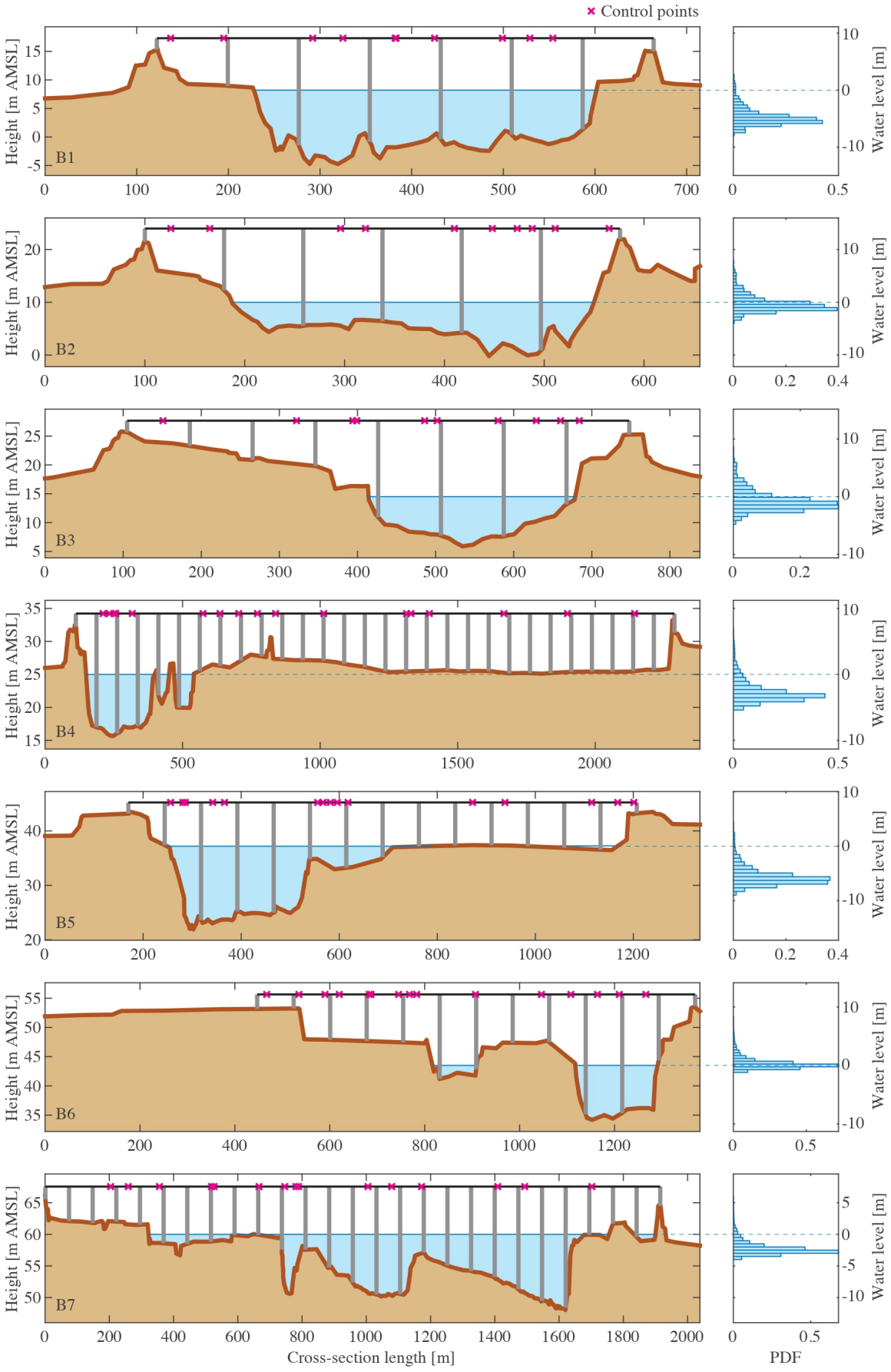

Figure 8. Cross-section profile of the selected bridges and probability density distribution of the water level (with respect to the sensor location) in the studied time interval.

$$\delta_{CP,ij} = \delta_i \left(1 - \frac{l_j}{l}\right) + \delta_{i+1} \left(\frac{l_j}{l}\right) \quad (8)$$

in which l_j is the distance between the first pier and the j-th control point. In this study, control points were randomly distributed across the bridges. Specifically, 10 control points were extracted from bridges B1s, B2s, and B3s, 15 control points were extracted from bridges B5s, B6s, and B7s, and 17 control points were extracted from bridge B4s. The entire datasets were simulated for both time intervals, I1 and I2, with a daily sampling period. A Gaussian white noise component with a standard deviation equal to 20% of that of the original signal was used to corrupt each displacement time history.

Fig. 10 compares real and simulated data of bridge B1 (and B1s) in time interval I1. Noteworthy, both temperature-driven oscillations and the negative peaks due to high water levels are qualitatively similar.

Modeled anomaly scenarios

As mentioned earlier, four distinct anomalous scenarios were simulated to test the procedure, namely, Sc, Se, Ou, and Up.

For the scouring effect (Sc), a temporary decrease in the support stiffness at the base of in-water piers was simulated. Specifically, the reduction was assumed to be proportional to the scouring depth, governed by the following relation:

$$k_s = k\left(1 - \alpha_s s\right) \quad (9)$$

where k_s is the reduced stiffness and $\alpha_s s$ is a reduction factor due to scour. This study assumes that this reduction is a linear function of the scour depth s, with $\alpha_s = 0.05$. The scour depth was calculated according to the HEC-18 technical report provided by the US Federal Highway Administration (64), which uses the following relation:

$$s = 2aK_1K_2K_3 \left(\frac{h_W}{a}\right)^{0.35} Fr^{0.43} \quad (10)$$

in which a is the pier width, while K_1, K_2, and K_3 are correction factors for pier nose shape, angle of attack of flow, and riverbed conditions, respectively. Moreover, Fr is the Froude number, defined as:

$$Fr = \frac{v}{\sqrt{gh_W}} \quad (11)$$

where v is the mean flow velocity and g is the acceleration of gravity. Here, the following parameters were assumed: $K_1 = 1$ (round-nose piers), $K_2 = 1$ (water flow perpendicular to the bridge section), and $K_3 = 1.1$ (clear-water scour) (54).

In this simulation, the pier width was considered the same for all bridges, with $a = 3.6m$, as reported by De Falco and Mele (63) for bridge B3. Additionally, the flow velocity was instantaneously estimated as $v = Q/A$, where Q represents the water discharge measured near the bridge locations (refer to Fig. 3), and A denotes the area of the flow cross-section, determined from water level data and topographic measurements (Fig. 8). The maximum flow velocities obtained through this method were approximately $2m/s$ during flood events, aligning well with specific studies conducted on the Po River. For instance, De Falco and Mele reported a velocity of $v = 2.28m/s$ during a flood event in October 1996 that impacted bridge B3. Similarly, Ballio et al. (65) reported a flow velocity of $3m/s$ for a motorway bridge near B3. The maximum stiffness reduction obtained in this way was approximately 30%.

For other anomalies, simpler modeling approaches were employed. Settlements (Se) and uplifts (Up) were simulated by vertically displacing the base of a single pier of the bridges downwards or upwards by 4mm, respectively. Conversely, for outliers (Ou), the displacement of a single control point was shifted (upwards or downwards) by 4mm. These displacement levels were selected to be realistically observable, given the millimeter-level accuracy of the real displacement datasets (49).

Fig. 11 shows a timeline of the simulated anomalies for the modeled bridges. Notably, simulated anomalies appear and disappear over time, i.e., with no permanent effects on the structures. While this approach may not reflect real-world scenarios, it is useful to validate the methodology. Specifically, it is assumed that bridge B1s underwent all four types of anomalies (identified through visual inspections), and the relevant datasets were labeled. Furthermore, B1s, B2s, and B5s experienced scouring due to a significant flooding event at the end of November 2019. Other simultaneous anomalies occurred between September and October 2020, during which B6s underwent uplift, while an outlier affected the data of B2s. Similarly, between September and November 2021, B4s and B7s experienced settlement and uplift, respectively.

Fig. 12 displays the data instances of simulated bridges between April 2 and June 30, 2020. As expected, the projected features of bridge B1s (affected by a settlement in a part of the considered interval) deviate from the centroid, demonstrating the effectiveness of the proposed anomaly index.

Anomaly detection and characterization

The methodology proposed in the paper was applied to the simulated datasets to evaluate its ability to detect the modeled anomalies. During the initialization phase, reference data from January 5, 2016, to November 13, 2019 (a period without simulated damage) was employed to build the projection matrices and establish the anomaly detection threshold. This threshold was set as the highest 99th percentile of the relative distance between all bridges and the centroid.

Subsequently, the anomaly index was computed for the monitoring interval (from November 13, 2019, to December 17, 2022). The resulting outcomes are presented in Fig. 13, where data points exceeding the threshold (indicated by the dashed horizontal line) are identified as anomalies. Noteworthy, most anomalies were successfully detected, with the index associated with scour particularly prominent. Specifically, the true positive rate (TPR), representing the proportion of instances exceeding the threshold during simulated damage, is 59.05%. Conversely, the false positive rate (FPR), which measures the proportion of instances above the threshold when no damage was simulated, is 1.31%. The relatively low TPR should be ascribed to the oscillations of the damage index within the anomalous intervals driven by the inherent variabilities of the environmental input. Nonetheless, as shown in Fig.

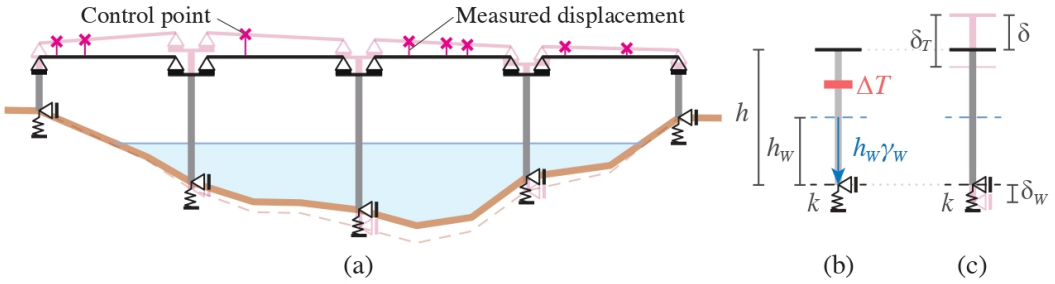

Figure 9. Simulated bridge model: (a) Bridge scheme; (b) Scheme of one pier and environmental actions; (c) Pier deformation.

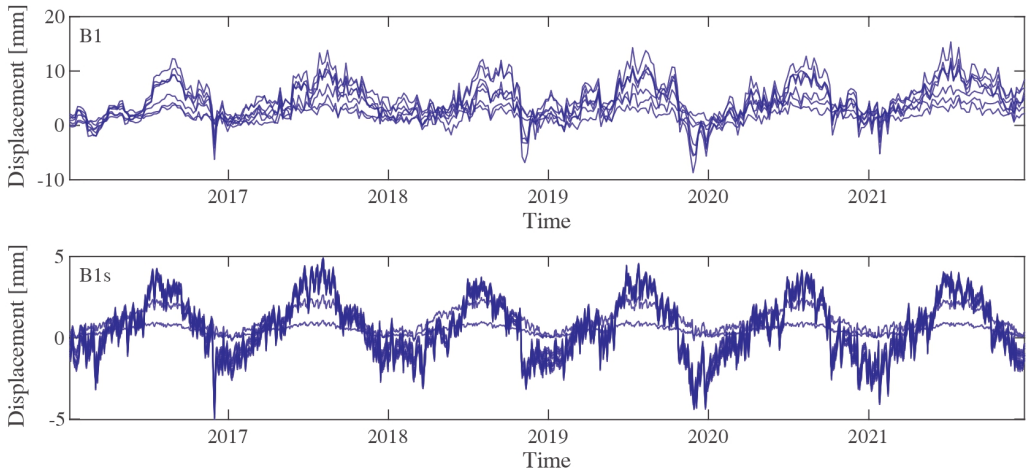

Figure 10. Time histories of the recorded displacements of B1 (top) and simulated displacements of B1s (bottom).

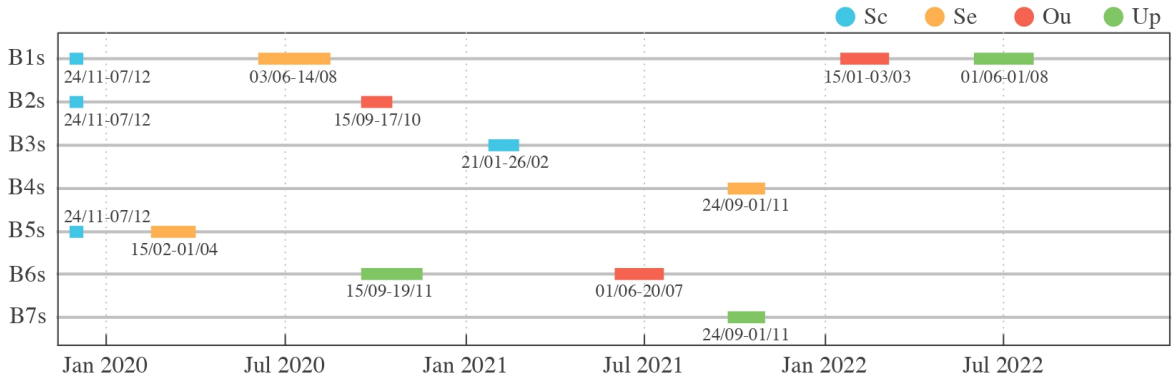

Figure 11. Timeline of simulated anomalies (dates in the format DD/MM).

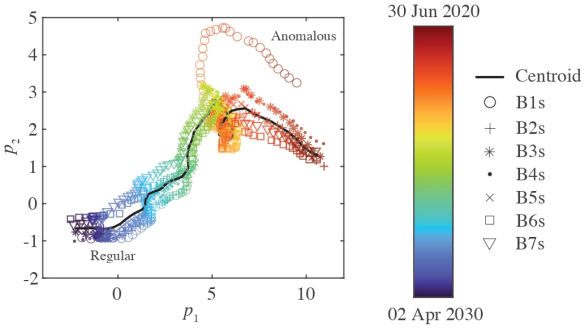

Figure 12. 2D representation of the simulated data in the latent domain between 2 Apr – 30 Jun, 2020.

13, clusters of positive data are clearly identifiable for all simulated anomalous events, proving the capabilities of the method to detect anomalous bridge conditions. Additionally, the low FPR reflects the low occurrence of false alarms.

The impact of each selected feature on the performance indices has been evaluated by recalculating the TPR and FPR after removing one feature at a time from the analysis. The effect of each feature on the TPR and FPR is reported in Tab. 2. Specifically, the mean (f_1), standard deviation (f_2), and skewness (f_3) of the displacement distribution, along with water level information (f_{10}), contributed the most to improving the TPR, though there was a slight decrease in TNR for features f_2 and f_{10}. Conversely, including feature f_8 negatively impacted the TPR due to its high variability but significantly reduced the FPR, with a decrease of the number

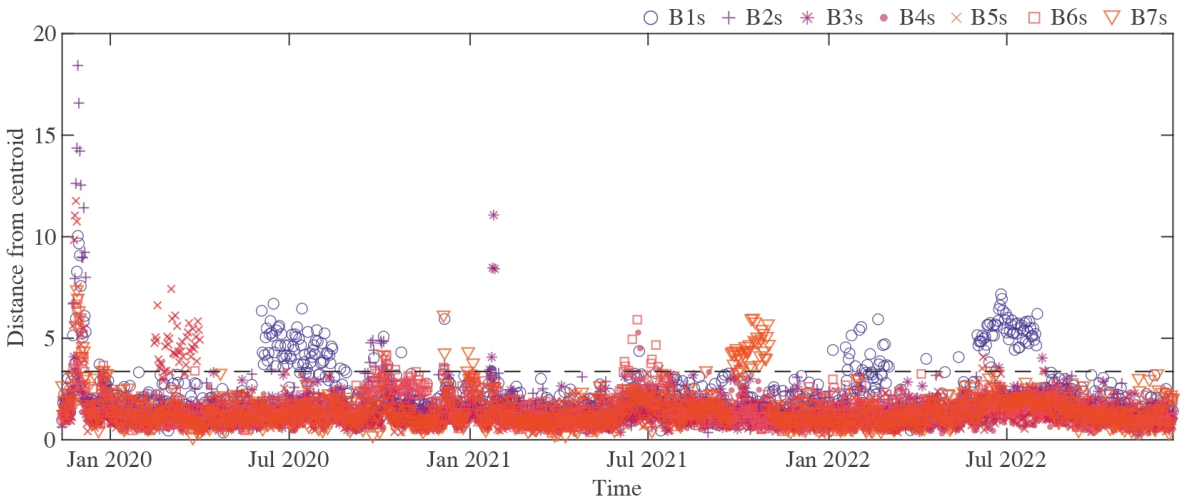

Figure 13. Anomaly index calculated over the analyzed time interval for the simulated bridges.

of false alarms of approximately 1/3. Features f_5, f_6, and f_7 had minimal impact on the performance metrics; however, they are still considered in this study since their inclusion does not affect computational complexity. Furthermore, the impact of these features on performance indices may vary depending on the specific case study. Thus, including these features could be beneficial for other applications.

The instances of B1s in the monitoring interval were then employed to train a SOM with 7×7 nodes connected in a hexagonal grid. The number of nodes was determined to have approximately 20 data instances in each neuron, thus ensuring statistical significance. Given that 1131 data instances were processed, around 56 nodes were required. A square grid (comprising 49 nodes) was chosen, as there was no prior knowledge about the feature distribution and hence no specific rationale for considering rectangular configurations. Fig. 14(a) shows the SOM structure and reports the number of instances classified in each node. The hexagons can be interpreted as portions of the source subdomain populated by the feature instances.

By feeding the SOM with different subsets of known anomalous instances, the regions to which they are assigned can be labeled accordingly. Specifically, Fig. 14(b)-(e) depict the classification outputs of the modeled anomalies, while Fig. 14(f) illustrates the regions occupied by the remaining "regular" data. It is interesting to note that the Sc, Se, and Up data populate distinct regions that are well separated from the regular data. Conversely, Ou occupies a broader portion of the feature space and, in some areas, overlaps with the regular data. Fig. 14(g) provides a synthesis of the obtained clusters, wherein the colors representing different anomalies have an intensity inversely proportional to the quantity of regular data that populates the regions.

Fig. 15 provides an overview of the classification outcomes resulting from inputting all available data into the SOM trained with B1s data. In this diagram, colored circles represent data instances allocated to regions assigned with the relevant labels. The circle size corresponds to the color intensity in Fig. 14(g). Additionally, black points denote anomalous data (i.e., exceeding the anomaly threshold) that were not categorized within any known labeled regions. These data may indicate false alarms or unknown anomalies. In these cases, visual inspections could be arranged to assess the affected structures and potentially assign new anomaly labels.

The results indicate successful detection and characterization of all simulated anomalies based on B1s labels, with the exception of bridge B4s during simultaneous anomalies in B7s. Additionally, a higher incidence of false alarms is observed when concurrent anomalies manifest, such as those occurring at the end of November 2019, in September-October 2020, and in September-October 2021. This can be attributed to the method used to determine the centroid, which excludes only one bridge from the calculation, assuming the realistic scenario of only one structure experiencing anomalies at a time. Furthermore, most false alarms remain unassigned to known labels or fall within regions also populated by regular data.

Simulation-to-real knowledge transfer

The same procedure, conducted within analogous reference and monitoring time intervals, was applied for anomaly detection using real data collected from bridges B1-B7. In this case, the data was projected onto the source subspace of B1s, the simulated bridge used as the source of information in the previous section. The link that allows projecting real data onto the simulated source domain and inferring anomaly information from it relies on the shared geometric characteristics and common environmental drivers (with comparable correlation coefficients) between the real and simulated configurations (66; 38).

Fig. 16 illustrates the anomaly index obtained over the monitoring time interval. Prominent peaks above the threshold were identified at the end of 2019 for bridges B1 and B2, while B2 exhibited a persistently high index throughout 2022. Additionally, short-term anomalies were detected for B3, B4, and B7, all of which were temporary.

Obtained results for anomaly classification are summarized in Fig. 17. While specific ground truth information for the analyzed bridges is unavailable, the classification labels suggest that the feature sets closely resembled those obtained in simulated scenarios during the identified anomalous intervals. Specifically, the anomalous events identified

Table 2. Impact of the selected features on anomaly detection performance metrics.

	f_1	f_2	f_3	f_4	f_5	f_6	f_7	f_8	f_9	f_{10}
ΔTPR	+6.38%	+10.49%	+10.70%	+1.03%	+0.41%	+0.00%	+0.20%	-11.73%	-1.44%	+3.91%
ΔFPR	-0.04%	+0.07%	-0.01%	-0.02%	-0.00%	-0.00%	-0.00%	-0.61%	-0.04%	+0.11%

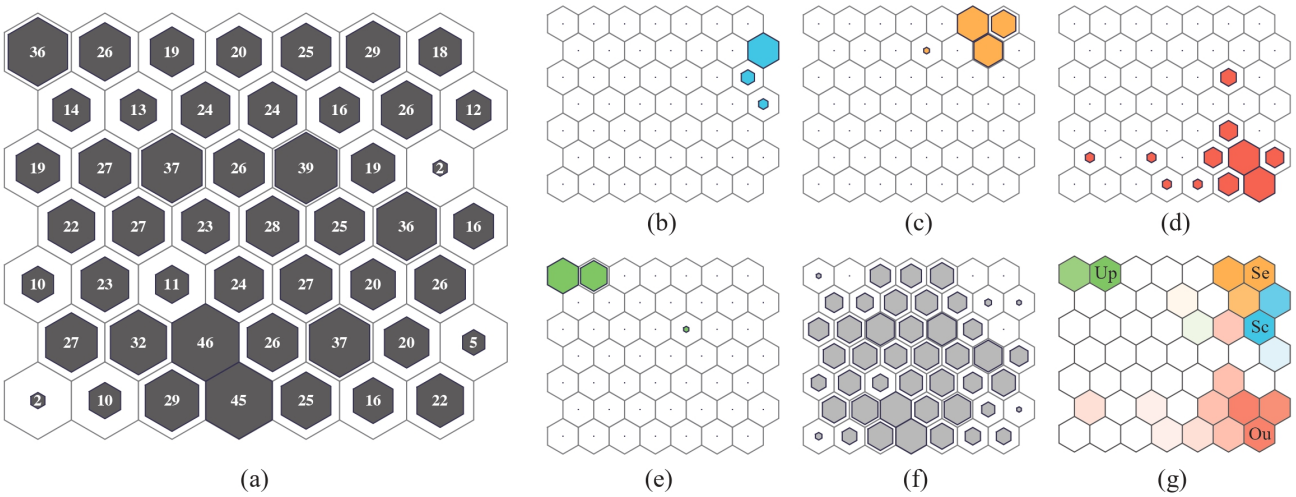

Figure 14. Data clustering for bridge B1s using the self-organizing map: (a) Distribution of data instances in the identified feature regions; Distribution of data selected in the intervals (b) 24 Nov 2019 – 07 Dec 2019, (c) 03 Jun 2020 – 14 Aug 2020, (d) 15 Jan 2022 – 03 Mar 2022, (e) 01 Jun 2022 – 01 Aug 2022, (f) the other time intervals; (g) Cluster labels.

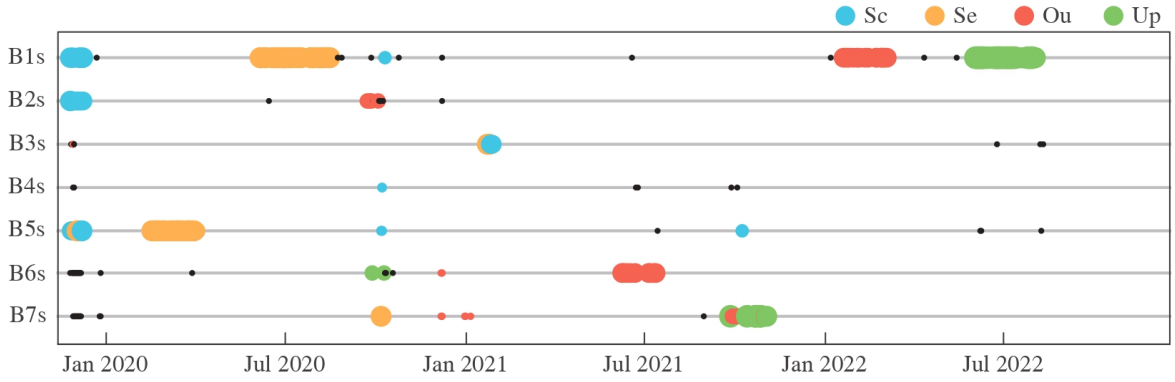

Figure 15. Classification of simulated data over the analyzed time interval.

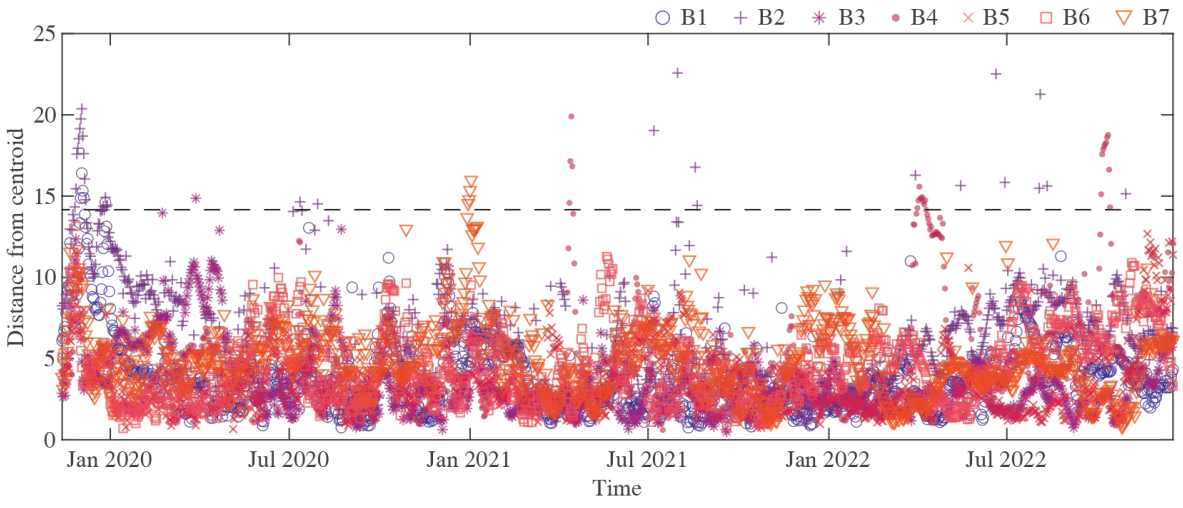

Figure 16. Anomaly index calculated over the analyzed time interval for the real bridges.

for bridges B1 and B2 at the end of November 2019 were classified as scour. Notably, monitoring agencies operating

in the region of the Po River reported severe flooding events during that period (67), which is also evident from the plot of water discharge in Fig. 3. ARPAE documented a significant flood event from November 22 to December 3, 2019, characterized by hydrometric levels exceeding "level 3" in all main sections of the river. In the ARPAE monitoring portal, "level 3" signifies the occurrence of an exceptional flood involving extensive erosion and sediment transport phenomena. The event was caused by a rainfall that persisted from November 21 to November 25, lasting 120 hours. Additionally, contributions to the flood were observed from snow melting in the Alps preceding and during the event.

Moreover, the recurrent anomalies identified for B2 in 2022 were classified as uplift. This phenomenon is more noticeable during summer, coinciding with certified severe drought conditions in the region (68). Specifically, this event led to an average river flow approximately 30% lower than the second-worst historical scenario ever recorded, an occurrence estimated to happen approximately once every 600 years. The prolonged drought may have contributed to the uplift observed in the riverbed near B2 during this period (69).

Other anomalies identified in the other bridges were shorter in duration and primarily categorized as uplift, settlements, and outliers.

Due to the black-box nature of the SOM and the lack of intuitive physical meaning for the projected features, it is challenging to identify in advance which specific measurement combination leads to a particular classification result. To help interpret the results, Fig. 18 shows the displacement time histories of B2 and B4, with highlighted intervals corresponding to anomalous events indicated by the relevant label colors. As expected, data labeled as scour exhibit a significant downward displacement of some control points within the river section. On the other hand, the uplifting event is characterized by a relative displacement of approximately 2 cm upwards in some control points with respect to the rest.

B4 also exhibits a brief period of uplift alongside instances of settlement and an outlier. While limited information is available for the identified uplift event, both the settlement and outlier anomalies appear to affect only a single control point. Consequently, both anomalies likely represent outlier occurrences. However, only the event at the end of 2022 is successfully classified as an outlier. In the anomaly identified in the first half of the year, the impact of the anomalous control point on statistical features might be comparatively lower than that used during the labeling process for outliers. Furthermore, the settlement label is justified by the downward shift of the anomalous control point. It is noteworthy that although the uplift event was identified for displacements similar to those of the outlier event, it was not labeled as an outlier, likely due to more than one control point displaying visibly anomalous displacements.

Conclusions

This paper introduced a novel methodology for detecting and classifying anomalies across multiple bridges within a geographical area using satellite-based InSAR data and environmental measures. The proposed method employs subspace alignment to harmonize bridge features, enabling the detection of anomalies based on changes in their relative behaviors. This approach changes the paradigm of traditional SHM for bridges, which typically relies on comparing each structure with itself from the past.

Simulated results underscore the feasibility of the proposed procedure, although challenges may arise when anomalies occur in multiple bridges simultaneously. These findings highlight areas for further investigation in future studies with a more advanced definition of the data centroid and anomaly threshold. Nevertheless, the simple methodology employed in this study demonstrates the potential of the proposed strategy.

Furthermore, the study investigates the transferability of knowledge acquired from simulated data to real-world bridge monitoring scenarios. The same alignment method used to minimize differences between real bridges is applied to reduce discrepancies between simulated and real data. By projecting real data onto the feature subspace of simulated bridges, the method attempts to classify real instances using simulated labels, yielding promising results. Notably, detected anomalies in real data align with documented instances from previous studies and technical reports.

Overall, the proposed approach has significant practical benefits for bridge monitoring agencies. It offers a cost-effective means of anomaly detection and characterization, leveraging free data. This approach can be integrated into strategies to enhance the resilience and safety of transportation infrastructure. Additionally, given the rapid advancements in satellite and data acquisition technologies, measurements with improved frequency and spatial resolution will soon become available, thereby further enhancing the potential of the regional-scale monitoring methodology outlined in this study.

Acknowledgements

Part of this study was carried out within the MOST – Sustainable Mobility National Research Center and received funding from the European Union Next Generation EU (PIANO NAZIONALE DI RIPRESA E RESILIENZA (PNRR) – MISSIONE 4 COMPONENTE 2, INVESTIMENTO 1.4 – D.D. 1033 del 17/06/2022, CN00000023). Part of this study was carried out within the SAT4SHM project – "Quantifying the effects of Structure-Soil-Structure interaction on structural modal parameters by combining Earth observation data with on-site dynamic monitoring: an enhanced vibration-based Structural Health Monitoring approach" -– funded by European Union, Next Generation EU within the PRIN 2022 PNRR program (D.D.1409 del 14/09/2022 Ministero dell'Università e della Ricerca). This manuscript reflects only the authors' views and opinions, and the Ministry cannot be considered responsible for them.

References

[1] C. S. Shim, N. S. Dang, S. Lon, and C. H. Jeon (2019), Development of a bridge maintenance system for prestressed concrete bridges using 3D digital twin model, *Structure and Infrastructure Engineering*, 15(10): 1319–1332.

[2] M. Jafari, A. Kavousi-Fard, T. Chen, and M. Karimi (2023), A review on digital twin technology in smart grid, transportation

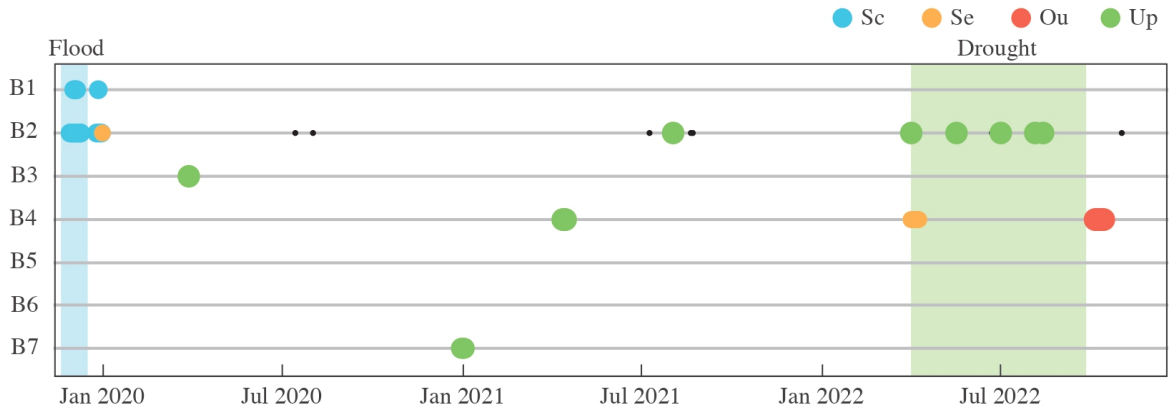

Figure 17. Classification of real data over the analyzed time interval. The highlighted intervals represent documented severe flood and drought events.

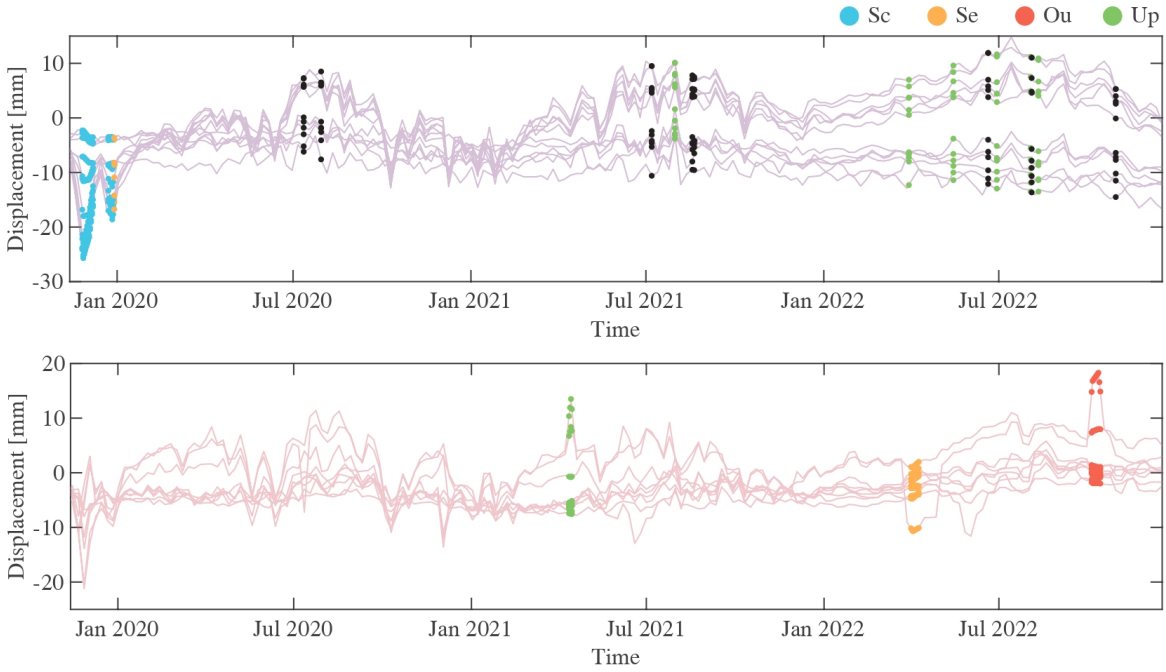

Figure 18. Displacement time histories of bridges B2 and B4 for interpretation of the assigned labels.

system and smart city: Challenges and future, *IEEE Access*, 11: 17471–17484.

[3] M. Mojtahedi, S. Newton, and J. Von Meding (2017), Predicting the resilience of transport infrastructure to a natural disaster using Cox's proportional hazards regression model, *Natural Hazards*, 85(2): 1119–1133.

[4] L. Sun, Z. Shang, Y. Xia, S. Bhowmick, and S. Nagarajaiah (2020), Review of bridge structural health monitoring aided by big data and artificial intelligence: From condition assessment to damage detection, *Journal of Structural Engineering*, 146(5): 04020073.

[5] C. Ferrante, L. B. Ciampoli, A. Benedetto, A. M. Alani, and F. Tosti (2021), Non-destructive technologies for sustainable assessment and monitoring of railway infrastructure: a focus on GPR and InSAR methods, *Environmental Earth Sciences*, 80(24): 806.

[6] D. Perissin (2016), Interferometric SAR multitemporal processing: Techniques and applications, *Multitemporal Remote Sensing: Methods and Applications*, 145–176.

[7] X. Liu, P. Wang, Z. Lu, K. Gao, H. Wang, C. Jiao, and X. Zhang (2019), Damage detection and analysis of urban bridges using terrestrial laser scanning (TLS), ground-based microwave interferometry, and permanent scatterer interferometry synthetic aperture radar (PS-InSAR), *Remote Sensing*, 11(5): 580.

[8] P. Milillo, G. Giardina, D. Perissin, G. Milillo, A. Coletta, and C. Terranova (2019), Pre-collapse space geodetic observations of critical infrastructure: The Morandi Bridge, Genoa, Italy, *Remote Sensing*, 11(12): 1403.

[9] F. Biondi, P. Addabbo, S. L. Ullo, C. Clemente, and D. Orlando (2020), Perspectives on the structural health monitoring of bridges by synthetic aperture radar, *Remote Sensing*, 12(23): 3852.

[10] S. Selvakumaran, S. Plank, C. Geiß, C. Rossi, and C. Middleton (2018), Remote monitoring to predict bridge scour failure using Interferometric Synthetic Aperture Radar (InSAR) stacking techniques, *International journal of applied earth observation and geoinformation*, 73: 463–470.

[11] J. Sousa, and L. Bastos (2013), Multi-temporal SAR interferometry reveals acceleration of bridge sinking before collapse, *Natural Hazards and Earth System Sciences*, 13(3): 659–667.

[12] E. Farneti, N. Cavalagli, M. Costantini, F. Trillo, F. Minati, I. Venanzi, and F. Ubertini (2023), A method for structural monitoring of multispan bridges using satellite InSAR data with uncertainty quantification and its pre-collapse application to the Albiano-Magra Bridge in Italy, *Structural Health Monitoring*, 22(1): 353–371.

[13] E. Farneti, N. Cavalagli, I. Venanzi, W. Salvatore, and F. Ubertini (2023), Residual service life prediction for bridges undergoing slow landslide-induced movements combining satellite radar interferometry and numerical collapse simulation, *Engineering Structures*, 293: 116628.

[14] A. Entezami, C. De Michele, A. N. Arslan, and B. Behkamal (2022), Detection of partially structural collapse using long-term small displacement data from satellite images, *Sensors*, 22(13): 4964.

[15] M. Del Soldato, R. Tomás, J. Pont Castillo, G. Herrera García, J. C. García Lopez-Davalillos, Ó. Mora, and others (2016), A multi-sensor approach for monitoring a road bridge in the Valencia harbor (SE Spain) by SAR Interferometry (InSAR).

[16] D. Peduto, F. Elia, and R. Montuori (2018), Probabilistic analysis of settlement-induced damage to bridges in the city of Amsterdam (The Netherlands), *Transportation Geotechnics*, 14: 169–182.

[17] G. Martin, A. Hooper, T. J. Wright, and S. Selvakumaran (2022), Blind source separation for MT-InSAR analysis with structural health monitoring applications, *IEEE Journal of Selected Topics in Applied Earth Observations and Remote Sensing*, 15: 7605–7618.

[18] Q. Huang, M. Crosetto, O. Monserrat, and B. Crippa (2017), Displacement monitoring and modelling of a high-speed railway bridge using C-band Sentinel-1 data, *ISPRS journal of photogrammetry and remote sensing*, 128: 204–211.

[19] E. J. Hoppe, F. Novali, A. Rucci, A. Fumagalli, S. Del Conte, G. Falorni, and N. Toro (2019), Deformation monitoring of posttensioned bridges using high-resolution satellite remote sensing, *Journal of Bridge Engineering*, 24(12): 04019115.

[20] D. Cusson, K. Trischuk, D. Hébert, G. Hewus, M. Gara, and P. Ghuman (2018), Satellite-based InSAR monitoring of highway bridges: Validation case study on the North Channel Bridge in Ontario, Canada, *Transportation Research Record*, 2672(45): 76–86.

[21] J. Zhao, J. Wu, X. Ding, and M. Wang (2017), Elevation extraction and deformation monitoring by multitemporal InSAR of Lupu Bridge in Shanghai, *Remote Sensing*, 9(9): 897.

[22] Q. Huang, O. Monserrat, M. Crosetto, B. Crippa, Y. Wang, J. Jiang, and Y. Ding (2018), Displacement monitoring and health evaluation of two bridges using Sentinel-1 SAR images, *Remote Sensing*, 10(11): 1714.

[23] M. Lazecky, I. Hlavacova, M. Bakon, J. J. Sousa, D. Perissin, and G. Patricio (2016), Bridge displacements monitoring using space-borne X-band SAR interferometry, *IEEE Journal of Selected Topics in Applied Earth Observations and Remote Sensing*, 10(1): 205–210.

[24] S. Selvakumaran, C. Rossi, A. Marinoni, G. Webb, J. Bennetts, E. Barton, S. Plank, and C. Middleton (2020), Combined InSAR and terrestrial structural monitoring of bridges, *IEEE Transactions on Geoscience and Remote Sensing*, 58(10): 7141–7153.

[25] D. Tonelli, V. F. Caspani, A. Valentini, A. Rocca, R. Torboli, A. Vitti, D. Perissin, and D. Zonta (2023), Interpretation of Bridge Health Monitoring Data from Satellite InSAR Technology, *Remote Sensing*, 15(21): 5242.

[26] M. Schlögl, P. Dorninger, M. Kwapisz, M. Ralbovsky, and R. Spielhofer (2022), Remote sensing techniques for bridge deformation monitoring at millimetric scale: Investigating the potential of satellite radar interferometry, airborne laser scanning and ground-based mobile laser scanning, *PFG–Journal of Photogrammetry, Remote Sensing and Geoinformation Science*, 90(4): 391–411.

[27] M. Schlögl, B. Widhalm, and M. Avian (2021), Comprehensive time-series analysis of bridge deformation using differential satellite radar interferometry based on Sentinel-1, *ISPRS Journal of Photogrammetry and Remote Sensing*, 172: 132–146.

[28] A. M. Alani, F. Tosti, L. B. Ciampoli, V. Gagliardi, and A. Benedetto (2020), An integrated investigative approach in health monitoring of masonry arch bridges using GPR and InSAR technologies, *NDT & E International*, 115: 102288.

[29] V. Macchiarulo, P. Milillo, C. Blenkinsopp, and G. Giardina (2022), Monitoring deformations of infrastructure networks: A fully automated GIS integration and analysis of InSAR time-series, *Structural Health Monitoring*, 21(4): 1849–1878.

[30] R. Lorenz, Y. Petryna, C. Lubitz, O. Lang, and V. Wegener (2024), Thermal deformation monitoring of a highway bridge: combined analysis of geodetic and satellite-based InSAR measurements with structural simulations, *Journal of Civil Structural Health Monitoring*, 14(5):1237–1255.

[31] A. Caprino, S. Puliero, F. Lorenzoni, M. Floris, and F. da Porto (2023), Satellite SAR Interferometry and On-Site Traditional SHM to Monitor the Post-Earthquake Behavior of the Civic Tower in L'Aquila (Abruzzo Region, Italy), *Remote Sensing*, 15(6): 1587.

[32] G. Bonaldo, A. Caprino, F. Lorenzoni, and F. da Porto (2023), Monitoring Displacements and Damage Detection through Satellite MT-InSAR Techniques: A New Methodology and Application to a Case Study in Rome (Italy), *Remote Sensing*, 15(5): 1177.

[33] D. Cusson, C. Rossi, and I. F. Ozkan (2021), Early warning system for the detection of unexpected bridge displacements from radar satellite data, *Journal of Civil Structural Health Monitoring*, 11(1): 189–204.

[34] K. DePrekel, E. H. Bouali, and T. Oommen (2018), Monitoring the impact of groundwater pumping on infrastructure using Geographic Information System (GIS) and Persistent Scatterer Interferometry (PSI), *Infrastructures*, 3(4): 57.

[35] J.R. Vázquez-Ontiveros, A.M. Ruiz-Armenteros, M.C. de Lacy, J.R. Gaxiola-Camacho, M. Anaya-Díaz, and G.E. Vázquez-Becerra (2023), Risk Evaluation of the Sanalona Earthfill Dam Located in Mexico Using Satellite Geodesy Monitoring and Numerical Modeling, *Remote Sensing*, 15(3):819.

[36] G.M. Guzman-Acevedo, G.E. Vazquez-Becerra, J.A. Quintana-Rodriguez, J.R. Gaxiola-Camacho, M. Anaya-Diaz, J.C. Mediano-Martinez, and F.J.C. Viramontes (2024), Structural health monitoring and risk assessment of bridges

integrating InSAR and a calibrated FE model, *Structures*, 63: 106353.

[37] Y. Zhou, G. Hao, J. Chen, J. Wei, and J. Zheng (2024), Long-term deformation monitoring of a steel-truss arch bridge using PSI technique refined by temperature field analysis, *Engineering Structures*, 311: 118164.

[38] J. Gosliga, P. A. Gardner, L. A. Bull, N. Dervilis, and K. Worden (2021), Foundations of Population-based SHM, Part II: Heterogeneous populations–Graphs, networks, and communities, *Mechanical Systems and Signal Processing*, 148: 107144.

[39] V. Giglioni, J. Poole, I. Venanzi, F. Ubertini, and K. Worden (2024), A domain adaptation approach to damage classification with an application to bridge monitoring, *Mechanical Systems and Signal Processing*, 209: 111135.

[40] S. J. Pan, and Q. Yang (2009), A survey on transfer learning, *IEEE Transactions on Knowledge and Data Engineering*, 22(10): 1345–1359.

[41] P. Gardner, X. Liu, and K. Worden (2020), On the application of domain adaptation in structural health monitoring, *Mechanical Systems and Signal Processing*, 138: 106550.

[42] J. Poole, P. Gardner, N. Dervilis, L. Bull, and K. Worden (2023), On statistic alignment for domain adaptation in structural health monitoring, *Structural Health Monitoring*, 22(3): 1581–1600.

[43] M. Omori Yano, E. Figueiredo, S. da Silva, and A. Cury (2023), Foundations and applicability of transfer learning for structural health monitoring of bridges, *Mechanical Systems and Signal Processing*, 204: 110766.

[44] E. Figueiredo, M. O. Yano, S. da Silva, I. Moldovan, and M. A. B. Mihai (2023), Transfer learning to enhance the damage detection performance in bridges when using numerical models, *Journal of Bridge Engineering*, 28(1): 04022134.

[45] E. Figueiredo, N. Peres, I. Moldovan, and A. Nasr (2024), Impact of climate change on long-term damage detection for structural health monitoring of bridges, *Structural Health Monitoring*.

[46] E. Figueiredo, G. Park, C.R. Farrar, K. Worden, and J. Figueiras (2011), Machine learning algorithms for damage detection under operational and environmental variability, *Structural Health Monitoring*, 10(6): 559–572.

[47] A. Entezami, H. Sarmadi, and B. Behkamal (2024), Removal of freezing effects from modal frequencies of civil structures for structural health monitoring, *Engineering Structures*, 319:118722.

[48] L. A. Bull, K. Worden, and N. Dervilis (2020), Towards semi-supervised and probabilistic classification in structural health monitoring, *Mechanical Systems and Signal Processing*, 140: 106653.

[49] *European Ground Motion Service*, https://egms.land.copernicus.eu/. Accessed: 2024-03-13. DOI: 10.2909/943e9cbb-f8ef-4378-966c-63eb761016a9.

[50] A. Ferretti, E. Passera, and R. Capes (2021), End-to-End Implementation and Operation of the European Ground Motion Service (EGMS): Algorithm Theoretical Basis Document, Tech. Rep. EGMS-D3-ALG-SC1-2.0-006. https://land.copernicus.eu/en/technical-library/egms-algorithm-theoretical-basis-document/@@download/file

[51] J. Muñoz-Sabater, E. Dutra, A. Agustí-Panareda, C. Albergel, G. Arduini, G. Balsamo, S. Boussetta, M. Choulga, S. Harrigan, H. Hersbach, and others (2021), ERA5-Land: A state-of-the-art global reanalysis dataset for land applications, *Earth System Science Data*, 13(9): 4349–4383.

[52] *Hydrographic monitoring - Interregional Agency for the Po River (AIPo)*, https://www.agenziapo.it/content/monitoraggio-idrografico-0. Accessed: 2024-03-13

[53] *Dext3r service - Regional Agency for Prevention, Environment and Energy of Emilia-Romagna (ARPAE)*, https://simc.arpae.it/dext3r/. Accessed: 2024-03-13

[54] M. Kosič, L. J. Prendergast, and A. Anžlin (2023), Analysis of the response of a roadway bridge under extreme flooding-related events: Scour and debris-loading, *Engineering Structures*, 279: 115607.

[55] C. Lin, C. Bennett, J. Han, and R. L. Parsons (2012), Integrated analysis of the performance of pile-supported bridges under scoured conditions, *Engineering Structures*, 36: 27–38.

[56] B. Fernando, A. Habrard, M. Sebban, and T. Tuytelaars (2013), Unsupervised visual domain adaptation using subspace alignment, in *Proceedings of the IEEE international conference on computer vision*, pp. 2960–2967.

[57] L. Ljung (1987), *System identification: Theory for the user*, (Prentice-hall, Inc.)

[58] G. Y. Kulikov and M. V. Kulikova (2013), Accurate numerical implementation of the continuous-discrete extended Kalman filter, *IEEE Transactions on Automatic Control*, 59(1): 273–279.

[59] V. Giglioni, I. Venanzi, V. Poggioni, A. Milani, and F. Ubertini (2023), Autoencoders for unsupervised real-time bridge health assessment, *Computer-Aided Civil and Infrastructure Engineering*, 38(8): 959–974.

[60] T. Kohonen (1982), Self-organized formation of topologically correct feature maps, *Biological Cybernetics*, 43(1): 59–69.

[61] E. Alhoniemi, J. Hollmén, O. Simula, and J. Vesanto (1999), Process monitoring and modeling using the self-organizing map, *Integrated Computer-Aided Engineering*, 6(1): 3–14.

[62] *Topographic measurements - Interregional Agency for the Po River (AIPo)*, http://geoportale.agenziapo.it/web/index.php/it/rilievi-topografici. Accessed: 2024-03-13

[63] F. De Falco and R. Mele (2002), The monitoring of bridges for scour by sonar and sedimetri, *NDT & E International*, 35(2): 117–123.

[64] L. A. Arneson (2013), Evaluating scour at bridges, Tech. Rep. United States. Federal Highway Administration.

[65] F. Ballio, G. Ballio, S. Franzetti, G. Crotti, and G. Solari (2018), Actions monitoring as an alternative to structural rehabilitation: Case study of a river bridge, *Structural Control and Health Monitoring*, 25(11): e2250.

[66] G. Delo, A. Bunce, E. J. Cross, J. Gosliga, D. Hester, C. Surace, K. Worden, and D. S. Brennan (2022), When is a bridge not an aeroplane? Part II: A population of real structures, in *European Workshop on Structural Health Monitoring*, pp. 965–974.

[67] G. Ricciardi and E. Comune (2019), Evento di piena del bacino del fiume Po - Novembre 2019, Tech.

Rep. ARPAE Emilia-Romagna - Struttura Idro-Meteo-Clima. https://allertameteo.regione.emilia-romagna.it/documents/20181/437770/Evento+piena+Po+novembre+2019/53e05c6b-1ee4-4104-a10c-f2370a4de4ca

[68] A. Montanari, H. Nguyen, S. Rubinetti, S. Ceola, S. Galelli, A. Rubino, and D. Zanchettin (2023), Why the 2022 Po River drought is the worst in the past two centuries, *Science Advances*, 9(32): eadg8304.

[69] A. A. Borsa, D. C. Agnew, and D. R. Cayan (2014), Ongoing drought-induced uplift in the western United States, *Science*, 345(6204): 1587–1590.